Far-Field Drag Extraction from Numerical Solutions and Wake Surveys

S. Esquieu*, M. Meheut†, H.F. von Geyr‡ and O. Brodersen§

Abstract

This paper focuses on ONERA drag extraction methods from numerical simulations and flow field wake surveys. A new far-field drag extraction software (FFD72) allows, thanks to its face-based data structure, to extract drag as well from structured (elsA cell-centered) as from unstructured (TAU cell-vertex) RANS solutions. By field analysis, this approach provides a drag breakdown into its physical components i.e. viscous drag, wave drag and lift-induced drag. To carry out such a drag breakdown from wind tunnel tests another method has been developed and allows the evaluation of these physical components from flow field wake measurements.

1 Introduction

Nowadays in aeronautics, aircraft design is driven by cost reduction, as well as regulation considerations. Indeed environmental constraints involve important reduction in emissions and noise. The answer can be obtained by improving the aircraft performance or by developing new aircraft configurations. Whatever the solution, the drag is a key point but its reliable prediction still remains one of the major challenges in aerodynamics [1]. Furthermore, the knowledge of this force is no longer sufficient for the designers, its phenomenological breakdown into its physical components (viscous, wave and induced drag) is also of great importance.

To overcome this problem, ONERA has developed original methods to determine the drag components from numerical solutions and from far-field wake measurements. Drag extraction from CFD calculations is very dependent on the mesh quality and computation accuracy. The far-field drag method allows to reduce the mesh dependency and ensures a more reliable drag prediction than the direct surface integration. This will be shown on transonic wing / body configuration computed with structured and hybrid unstructured approaches. Special attention will be devoted to the whole aerodynamic assessment process : mesh generation, CFD computation and post-processing. The original method to determine the drag components from far-field wake measurements will be presented on a high-lift configuration in landing conditions and will be compared with post-processing of hybrid unstructured computations.

*Research Engineer, ONERA

†PhD Student attached to the Université de Sciences et Technologies de Lille, ONERA

‡Research Engineer, DLR

§Research Engineer, DLR

2 Drag extraction from numerical solutions

Drag can be extracted from a numerical flow solution either by surface integration or through a field analysis.

2.1 Near-field drag

The former technique is straightforward and available in all aerodynamics codes. It gives a mechanical breakdown of the drag into its normal (pressure) and tangential (friction) components.

The **near-field drag** can be expressed as :

$$D = D_p + D_f = \int_{S_A} [(p - p_\infty) n_x - (\vec{\tau_x}.\vec{n})] dS \qquad (1)$$

where S_A is the aircraft surface, $\vec{n}$ the outward (relative to the flow field) unit normal vector (as shown in Fig.1) and $n_x = \vec{n}.\vec{i}$ with $\vec{i}$ the unit vector in the free-stream flow direction, p the pressure and $\vec{\tau_x}$ the vector of viscous deviatoric stresses of components $(\tau_{xx}, \tau_{xy}, \tau_{xz})$, x being the free-stream direction.

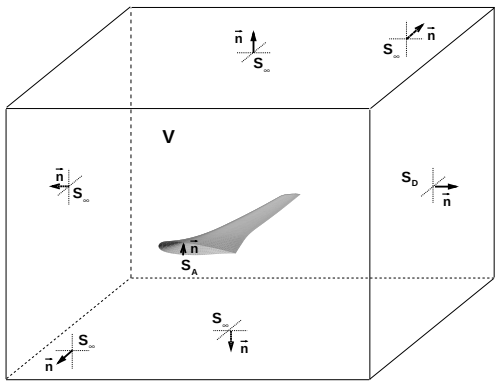

Figure 1: Control volume V.

2.2 Far-field drag

The ONERA method for far-field drag extraction from numerical solutions follows a formulation recently introduced by van der Vooren [2] and discussed by Destarac in [3].

This technique is based on a far-field analysis and the theoretical basis of the far-field drag computation and breakdown is the use of the momentum theorem and mass conservation (see detailed presentation in [3] [4]) which leads to the use and decomposition of vector $\vec{f}$:

$$\vec{f} = -\rho(u-u_\infty)\vec{q} - (p-p_\infty)\vec{i} + \vec{\tau_x} \tag{2}$$

where ρ is the density and $\vec{q}$ the velocity.

With this theory, distinction must be made between thermodynamic irreversible process (viscous drag and wave drag production) and reversible process (induced drag production). By selecting zones in the field, it may give a phenomenological breakdown of drag [**?**], [7] into physical drag sources : wave drag, viscous drag and lift-induced drag. The physical breakdown of drag is considered as more useful than the mechanical, by design engineers.

Field quantities involved in this far-field technique are based on the velocity defect $\Delta\overline{u} = u - u_\infty$ which can be written as :

$$\Delta\overline{u} = u_\infty \sqrt{1 + \frac{2\Delta H_i}{{q_\infty}^2} - \frac{2[(e^{\frac{\Delta s}{r}})^{(\frac{\gamma-1}{\gamma})} - 1]}{(\gamma-1){M_\infty}^2}} - u_\infty \tag{3}$$

where Δs and ΔH_i are the entropy and the stagnation enthalpy relative to the free-stream values, M the Mach number, γ the ratio of specific heat and r the gas constant, ∞ denotes the free stream state.

2.2.1 Viscous and wave drag

Viscous and wave drag are due to irreversible phenomena which imply a change in energy form and so it is convenient to define the vector $\vec{f_{vw}}$ relative to the irreversible drag productions :

$$\vec{f_{vw}} = -\rho\Delta\overline{u}\vec{q} \tag{4}$$

The theory is based on the assumption that production of viscous drag and wave drag is confined to finite control volumes V_V (boundary layers and viscous shear layers) and V_W (shock layers), and that the flow can be considered as inviscid outside these volumes (see Fig.2). If V_v and V_w can be defined without overlap, wave and viscous drag can be expressed as :

$$D_v = \int_{V_v} div\vec{f_{vw}} dV \tag{5}$$

$$D_w = \int_{V_w} div\vec{f_{vw}} dV \tag{6}$$

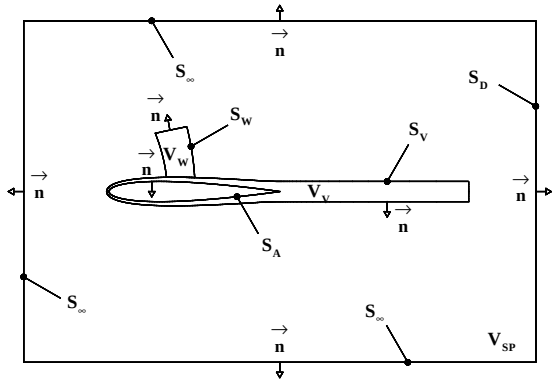

Figure 2: Boundaries and control volumes for far-field drag breakdown.

Besides, numerical schemes and truncation error inherent to CFD-codes produce artificial (spurious) drag which has to be removed to make an accurate prediction of drag. Thanks to the far-field method, the non-selected zones of irreversible drag production are related to spurious drag. So, numerical effects do not affect the far-field drag values and a more accurate drag extraction can be obtained. This is an asset of the method because direct surface force integration given by aerodynamics codes cannot distinguish spurious contributions to drag from physical production.

2.2.2 Physical criteria for viscous and wave drag detection

To detect shock layers, Tognaccini and Paparone [5] proposed the following physical sensor :

$$F_{shock} = \frac{\vec{q}.\vec{\nabla}p}{a|\vec{\nabla}p|} \tag{7}$$

with p the pressure and a the local sound speed.

Boundary layers detection and selection are based on a cut-off of a norm of the viscous deviatoric stresses $[\tau]$ that varies through the local boundary layer thickness.

$$F_{bl} = \frac{[\tau]}{[\tau_{medium}]} \tag{8}$$

Viscous shear layers are detected following a criterion proposed by Tognaccini [6] using the ratio of turbulent to molecular viscosity.

$$F_{vsl} = \frac{\mu_l + \mu_t}{\mu_l} \tag{9}$$

2.2.3 Lift-induced drag

Lift-induced drag is related to reversible phenomena which involve only exchange of mechanical energy.

Transverse kinetic energy is added to the flow downstream of lifting finite surfaces.

For the definition of induced drag, it is convenient to create a third vector $\vec{f_i}$ such that :

$$\vec{f} = \vec{f_{vw}} + \vec{f_i} \tag{10}$$

$$\vec{f_i} = -\rho(u - u_\infty - \Delta\overline{u})\vec{q} - (p - p_\infty)\vec{i} + \vec{\tau_x} \tag{11}$$

The formula proposed by van der Vooren for induced drag [2] in the case of a non-propelled aircraft is :

$$D_i = \int_{V_i} div\vec{f_i} dV - \int_{S_A} (\vec{f_i}.\vec{n}) dS \tag{12}$$

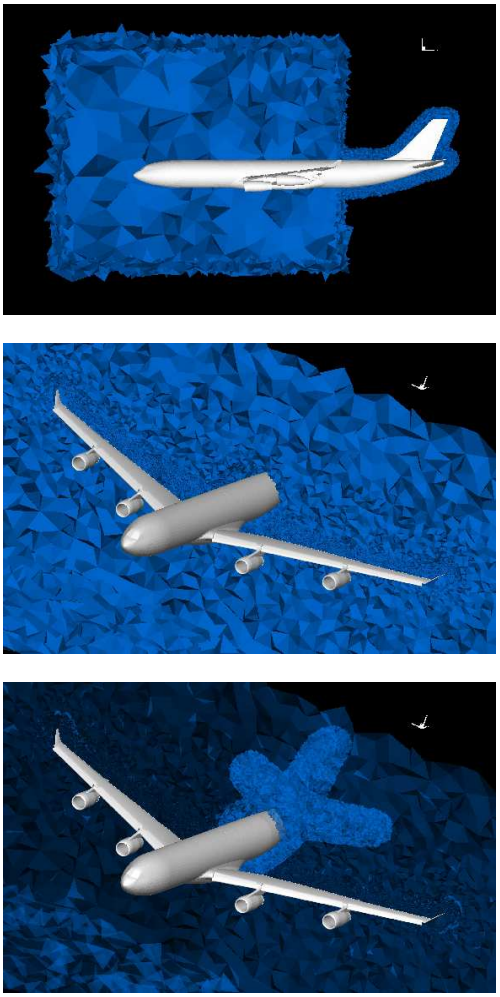

Figure 3: Lift-induced drag integration volume V_i- Downstream surface just behind the wing - Tail plane volume.

It can be shown [2] that in the volume integral, the volume of the computational domain V_i can be theoretically replaced by $(V_v \cup V_w)$, or, if numerical spurious drag sources are present in the field by $(V_v \cup V_w \cup V_{sp})$, where V_{sp} is a volume containing the spurious drag sources. A volume which ensures the previous recommendations for the lift-induced drag integration is presented in figure 3.

It is important to notice that in numerical solutions of lifting flow problems, the transverse kinetic energy decreases downstream of the body at a much faster rate than in reality [7] [8] because of numerical diffusion of wing tip vortices.

In comparison to other formulations, lift-induced drag is not computed as a surface integral over a downstream surface (Trefftz plane) but in a volume including the viscous part of the flow and the shock layers and excluding the wing tip vortices as shown in figure 3. Lift-induced drag is due to a reversible phenomenon related to the crossflow velocity components $\Delta v^2 + \Delta w^2$ (approximation of vector $\vec{f_i}$ with small perturbation assumptions) and its numerical diffusion (to be added to the previous part) is an irreversible phenomenon (related to vector $\vec{f_{vw}}$). Van der Vooren's formulation is such that these two contributions computed in a same volume containing the wing tip vortices are equal and of opposite sign. This is the reason why volume V_i does not include the wing tip vortices.

2.3 Drag extraction on a transonic configuration

In the framework of the DLR-ONERA MIRACLE project, the AS28G wing / body configuration (Garteur AG39) was computed at cruise conditions with the structured ONERA-elsA code and the unstructured DLR-TAU code.

Thanks to its face-based structure, which operates on arbitrary meshes and for different discretization techniques, such as cell-centered or cell-vertex, the numerical drag extraction software FFD72 was used in order to analyze the quality of the flow solutions obtained with two different codes (elsA-structured and TAU-hybrid) in terms of drag prediction, to investigate the influence of different parameters (number of grid points, artificial viscosity, mesh adaptation) on the flow and to compare different type of meshes (structured and hybrid) [9]

In order to realize a thorough validation, particular attention was given to the three successive steps of the aerodynamic assessment process : mesh generation, CFD computation and post-processing for both approaches.

2.3.1 Structured and hybrid grids

The structured grid (Fig.4) was realized with ICEM Hexa and the hybrid mesh (Fig.5) with CentaurSoft software. Particular effort was made to generate high

quality structured (around 6 millions points) and hybrid (around 3 millions nodes and 10 millions elements) grids in order to obtain accurate solutions.

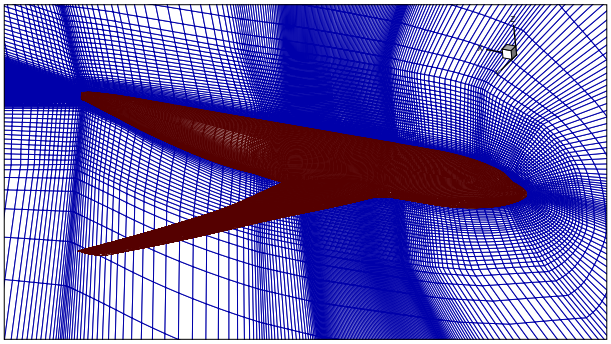

Figure 4: AS28G Wing / Body configuration - Multi-block structured mesh (48 blocks).

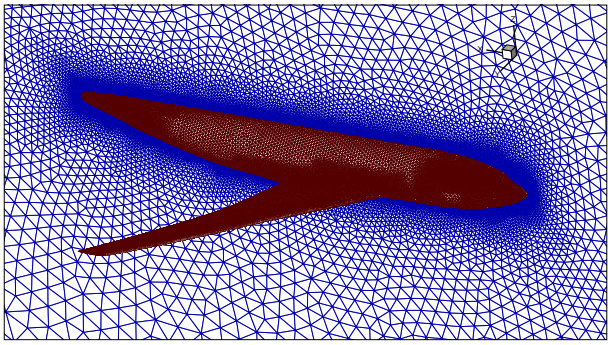

Figure 5: AS28G Wing / Body configuration - Hybrid mesh.

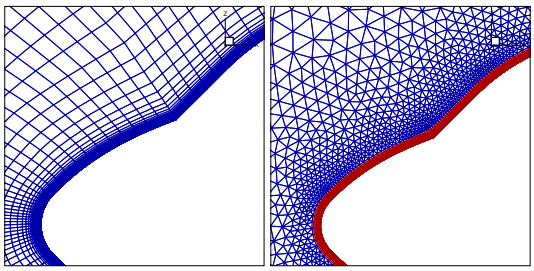

Figure 6: AS28G Wing / Body configuration - Structured and hybrid mesh around the fuselage nose.

Hexahedral and prismatic boundary layers (35 prism layers) are presented in the figure 6 around the fuselage nose. Concerning the hybrid grid, special attention to obtain a smooth transition between prismatic and tetrahedral elements was considered in order to avoid numerical perturbations which are directly responsible for spurious drag productions.

2.3.2 CFD computations

The aerodynamic conditions considered for this AS28G wing / body configuration [14] are : $M = 0.80$, $CL = 0.50$ and $Re_c = 10.4\ 10^6$ with $c = 0.94081m$.

Structured RANS computations were performed with the ONERA object-oriented software elsA [11] [10] which uses a cell-centered finite-volume discretization on structured multi-block meshes. Hybrid RANS computations were realized with the finite volume vertex-based DLR-TAU-code [12] [13] and two mesh adaptation steps (solution TAU(ad.2)) were conducted during the convergence process. Jameson scalar dissipation was used in both approaches. Implicit time integration has been applied with the elsA code while explicit Runge-Kutta scheme was used to reach the steady state with the TAU code. Both computations were performed with the Spalart-Allmaras turbulence model.

	α	CL	CD_p	CD_f	CD_{nf}
ETW	1.70	0.499	-	-	255.5
elsA	1.80	0.501	152.1	96.5	248.6
TAU(ad.2)	2.00	0.500	157.8	89.4	247.2

Table 1: AS28G Wing / Body - ($M = 0.80, Re_{/c} = 10.4\ 10^6$) - Lift coefficients and near-field drag values.

As presented in table 1, in both cases the RANS computations underestimate the drag coefficient of about 7. to 8. drag counts in comparison to ETW wind tunnel tests.

Fig.7 presents a comparison of the pressure distributions obtained in cruise conditions in ETW and with the CFD codes. A satisfying agreement is obtained with the experimental results.

A general trend was identified concerning the near-field drag values, good agreement on the sum of the pressure and friction drag but non negligible scatter between these two components when taken separately.

2.3.3 Far-field drag analysis

As indicated previously, physical criteria allow to detect the viscous and wave drag productions within the flow field. Figure 8 shows the viscous (in grey) and wave (in red) drag integration volumes respectively for the structured and the hybrid solutions. The resulting drag breakdown is presented in table 2.

The far-field drag values show a slight discrepancy on the wave drag component and a significant one on the viscous drag component between elsA and TAU solutions while a good agreement is obtained for the lift-induced drag component. It is interesting to notice that the viscous pressure drag ($CD_{vp} = CD_v - CD_f$) exhibits a scatter of only 2.2 drag counts between elsA and TAU solutions with a higher value of the angle of attack in the

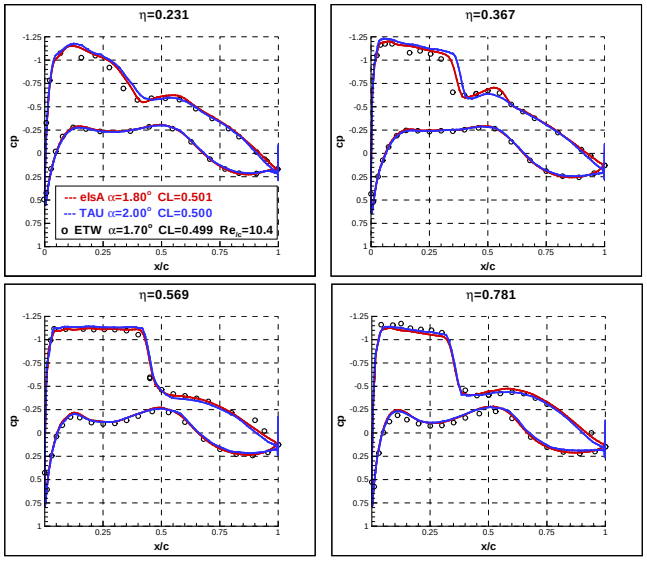

Figure 7: AS28G Wing / Body configuration - ETW / elsA / TAU - Cross-sectional comparisons of the pressure distributions.

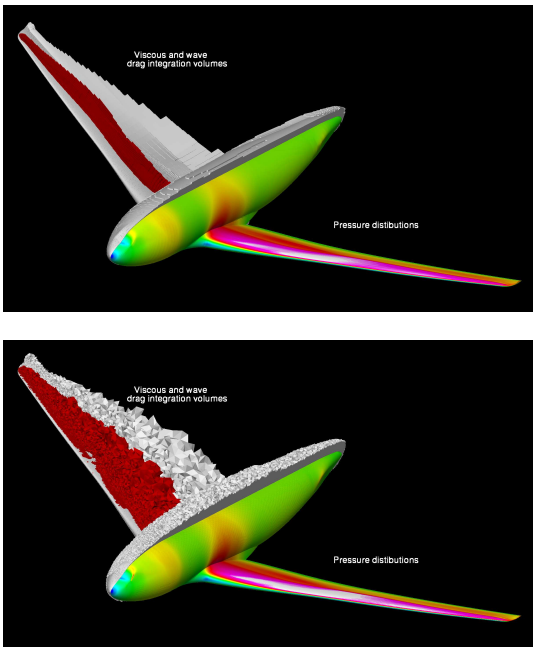

Figure 8: AS28G wing / body configuration - Structured v.s. Hybrid - Pressure distributions - Viscous and wave integration volumes from FFD72

last case. The limited level of spurious drag in the two cases confirms the good quality of the meshes and points out the efficiency of the two mesh adaptation steps for the hybrid case.

Thanks to its cell-by-cell approach [15], [16], the method allows the visualization of all irreversible drag sources, spurious as well as physical, throughout the flow field (see Fig.9) with in grey the boundary layers and the

FFD72	CD_w	CD_v	CD_i	CD_{ff}	CD_{sp}
elsA	13.2	137.4	95.0	**245.6**	3.0
TAU(ad.2)	15.5	132.5	94.3	**242.3**	4.9

Table 2: AS28G Wing / Body - ($M = 0.80, Re_{/m} = 11.0\ 10^6$) - Drag breakdown.

wake, and in red the shock wave with its location along the wing span. The non-selected zones of irreversible drag production (outside detected physical zones in grey and in red in Fig.9) are related to spurious drag. So, numerical effects do not affect the far-field drag values and a more accurate drag extraction can be obtained. This is an asset of the method because direct surface force integration given by aerodynamics codes cannot distinguish spurious contributions to drag from physical production and spurious drag is systematically included in the pressure drag (see demonstration in the following section).

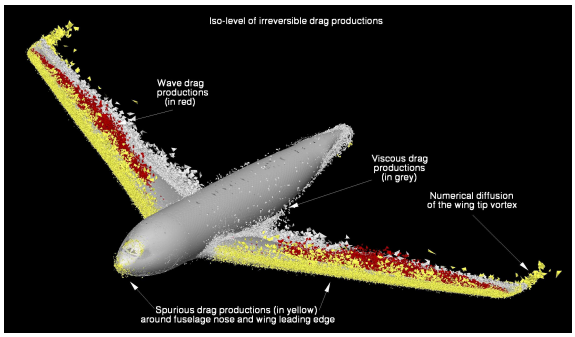

Figure 9: AS28G WB - Hybrid mesh / TAU computation - Physical and numerical irreversible drag sources.

2.3.4 Discussion on spurious drag and overestimation of pressure drag (demonstration in structured approach)

The drag extraction technique provides a useful and instructive drag breakdown but can also be used as an expertise-tool to evaluate the quality of the meshes and solutions within the whole drag prediction process.

For this demonstration, we make a comparison between the previous structured fine mesh (see Fig.4) and a Patched Grid mesh which was generated on the basis of this fine one by using partially coincident frontiers. This technique allows to keep a very good refinement in all the physical zones of the flow such as viscous layers, shocks or wing tip vortices and permits to reduce the number of points in the far-field (about 33% points saved in this case). The topology of the refined blocks is presented in figure 10 knowing that all the other blocks are coarsened using 1/2 partially coincident connections as presented around the fuselage

nose in figure 11.

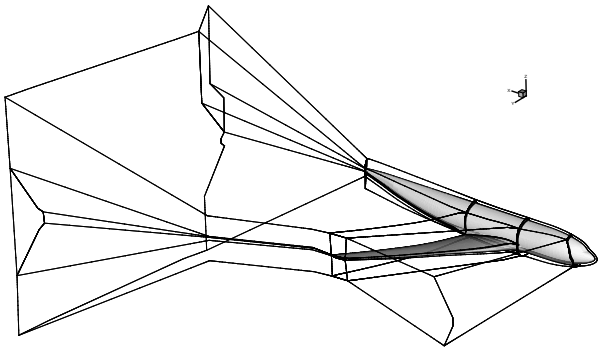

Figure 10: AS28G wing / body configuration - Patched Grid mesh - Topology of the refined blocks

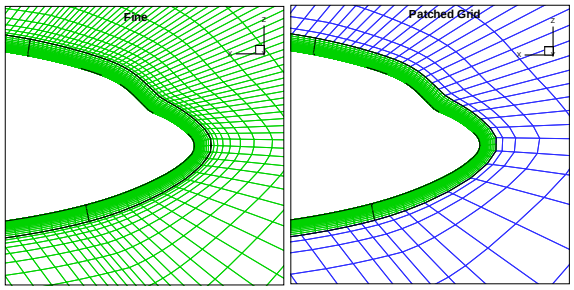

Figure 11: AS28G wing / body configuration - Structured coincident and Patched Grid meshes

In this case, the CFD computations were performed with the following aerodynamic conditions $M = 0.80$, $AoA = 2.2\,\text{deg}$ and $Re_c = 10.410^6$.

The near-field and far-field drag values are presented in table 3. The near-field drag value is higher (9.2 drag counts) in the Patched-Grid case than in the fine one because of an overprediction of the pressure drag.

The far-field drag breakdown shows different levels of spurious drag for each calculation : 5.1 drag counts in the fine case and 17.1 in the Patched Grid case. However, wave and viscous drag are in close agreement between the Patched Grid and the fine computations. It appears a difference of 2.2 drag counts between the two calculations which can be explained, firstly by a slightly lower lift coefficient in the Patched Grid case, and secondly by the partially coincident frontier located near the wing tip vortex (see Fig.10) which may modify the intensity of the transverse kinetic energy.

Thanks to the spurious drag separation, the far-field drag values obtained on the two solutions are in better agreement than the near-field drag values. Although Patched Grid is a particular kind of multi-block structured mesh, we can conclude here that the quality of the mesh has a greater impact on the near-drag values than on the far-field drag values.

	CL	CD_p	CD_f	$CD_p + CD_f$
Fine	0.549	194.3	96.6	290.9
PG	0.547	203.5	96.4	299.9

	CD_w	CD_v	CD_i	CD_{ffd}	CD_{sp}
Fine	26.0	149.7	110.1	285.8	5.1
PG	25.0	150.0	107.9	282.9	17.1

Table 3: Near-field and far-field drag values.

An exhaustive analysis of the field exhibits a larger non-physical entropy creation (spurious drag productions) around the fuselage nose in the Patched Grid case than in the fine one as shown in Fig.12.

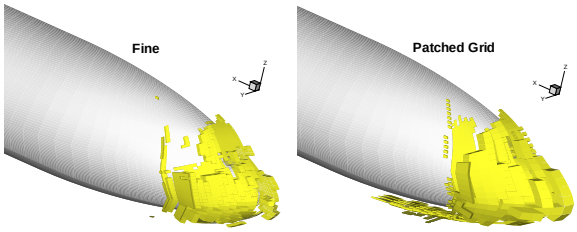

Figure 12: AS28G wing / body configuration - Structured coincident and Patched Grid meshes - Iso-level of spurious drag productions (in yellow)

To make the link between spurious drag productions and over-prediction of pressure drag, the top illustration in figure 13 presents the evolution of the friction and pressure drag when progressively added on each aircraft surface panel. This clearly demonstrates that no difference, between the two solutions, appears for the friction drag at the skin of the configuration but concerning the pressure drag : panels 5, 6 and 7 are responsible of 6 pressure drag counts of over-estimation while panels 8 to 12 lead produce 3 drag counts more in the patched Grid case than in the fine one (see bottom graphic in Fig.13).

So, the near-drag value, especially the pressure drag, is in close link with the quality of the mesh. In this case, the brutal change in cell sizes around the fuselage nose which is a region of high velocity gradients (nevertheless in “inviscid region” because outside the boundary layer) is responsible of large spurious drag productions. In the general case, the spurious productions are located around the stagnation points (leading edge, fuselage nose, nacelle lips, ...) where the pressure gradients are very high and the meshes not enough refined in these large curvature zones. As a consequence, the surface pressure exerted on the body is modified and the equilibrium between the front and the back parts of the configuration is slightly changed leading to different pressure drag values on solutions obtained with different

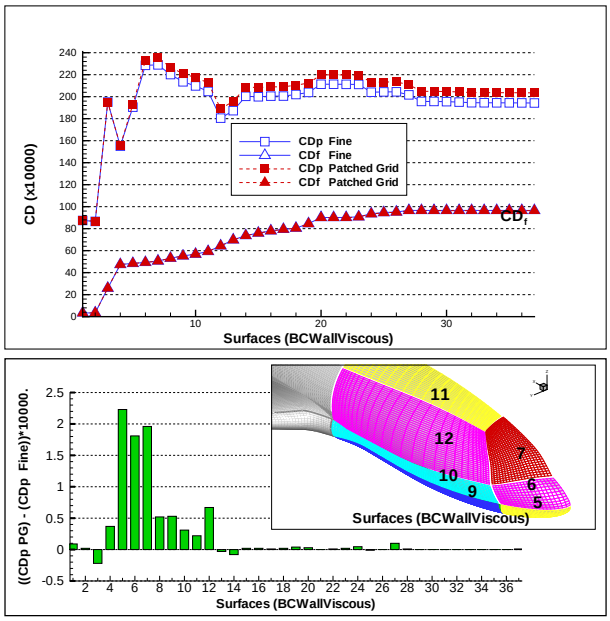

Figure 13: AS28G wing / body configuration - Structured coincident and Patched Grid meshes - Identification of over-estimation of pressure drag

grids for a same configuration.

So, this demonstration points out the importance of the mesh quality in the drag extraction process and confirms that for an accurate resolution it is necessary to ensure an excellent refinement in all the complex parts of the flow, not only in zones containing physical phenomena which generate drag but also inviscid high gradients regions. So within the whole drag extraction process, it is necessary to generate a good quality initial mesh for the structured approach (because no mesh quality improvements afterwards) and to use the mesh adaptation procedure to improve the grid quality in the unstructured case, even so, thanks to the far-field drag method the sensitivity to the mesh quality is reduced because of spurious drag elimination.

3 Drag extraction from wake surveys

Although the accuracy of CFD computations is constantly increasing, wind tunnel tests still remain a key element to make a reliable evaluation of the drag components. However, the physical breakdown from wake surveys is a challenge. Indeed in a wind tunnel, the forces acting on a model are determined using balance measurements which provides very accurate results but prevents any physical breakdown.

To overcome this problem, ONERA has developed an original method to determine the drag components from far-field wake measurements [17, 18]. It consists in writing profile (viscous and wave contributions) and induced components in terms of flow variables measured inside the wake, downstream of the model. To guarantee an accurate phenomenological drag breakdown in all configurations, an analysis of the drag sources is carried out.

3.1 Drag breakdown methods

3.1.1 Far-field approach

The far-field approach is based on an integration of the momentum equation inside a closed volume surrounding the model (figure 14) and consists in writing the drag in terms of wake variables, contrary to the near-field approach which is an integration over the surface of the configuration. The domain of integration can be reduced to the downstream plane Σ_1 using realistic assumptions on Σ_{lat} and Σ_∞. The drag coefficient is :

$$C_D = \frac{2}{S_{ref}} \int_{\Sigma_1} \left[\left(\frac{P_\infty - P}{\rho_\infty U_\infty^2} \right) + \frac{\rho}{\rho_\infty} \frac{U}{U_\infty} \left(1 - \frac{U}{U_\infty} \right) \right] ds \quad (13)$$

S_{ref}, P, P_∞, ρ, ρ_∞, U and U_∞ are respectively the reference surface, the local and upstream static pressures, densities and axial velocities ($U = \vec{V}.\vec{x}$, $\vec{V} = (U, v, w)$ and $\vec{U_\infty} = U_\infty.\vec{x}$).

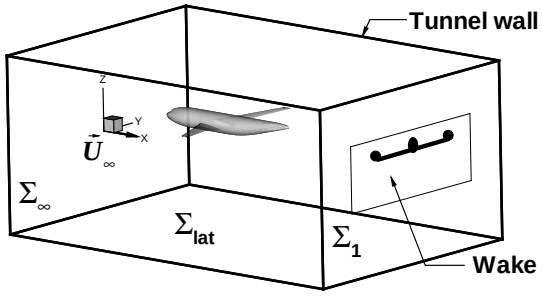

Figure 14: Profile drag.

The drag coefficient can also be written in terms of wake variables as :

$$C_D = \frac{2}{S_{ref}} \int_{\Sigma_1} \left[\frac{1}{\gamma M_\infty^2} \left(1 - \frac{P_i}{P_{i\infty}} \Im^{\frac{\gamma}{\gamma-1}} \right) + \frac{T_{i\infty}}{T_i} \frac{P_i}{P_{i\infty}} \Im^{\frac{1}{\gamma-1}} \frac{U}{U_\infty} \left(1 - \frac{U}{U_\infty} \right) \right] ds \quad (14)$$

M_∞, γ, P_i, $P_{i\infty}$, T_i and $T_{i\infty}$ are respectively the upstream Mach number, the ratio of specific heats, the local and upstream stagnation pressures and temperatures. $\Im$ is defined by :

$$\Im = 1 + \frac{\gamma - 1}{2} M_\infty^2 \left(1 - \frac{V^2}{U_\infty^2} \frac{T_{i\infty}}{T_i} \right) \quad (15)$$

3.1.2 Asymptotic drag formulation

The formulation developed at ONERA is based on the small perturbations assumption. Assuming that the downstream states differ only slightly from the upstream ones :

$$\left\{ \begin{array}{l} P_i = P_{i\infty}\left(1+\delta P_i\right) \\ T_i = T_{i\infty}\left(1+\delta T_i\right) \\ \vec{V} = U_\infty\left(\left(1+\delta u\right)\vec{i} + \delta v\vec{j} + \delta w\vec{k}\right) \end{array} \right. \tag{16}$$

with δP_i, δT_i, δu, δv and $\delta w << 1$. From a second order asymptotic development of the drag expression (14):

$$\begin{aligned} C_D &= \frac{1}{S_{ref}}\int_{Wake}\left[-\frac{2}{\gamma M_\infty^2}\delta P_i - \delta T_i \right. \\ &\quad \left. + \left(1-\frac{M_\infty^2}{4}\right)\delta T_i^2 - \delta P_i \delta T_i\right] ds \\ &\quad + \frac{1}{S_{ref}}\int_{\Sigma_1}\left[\delta v^2 + \delta w^2 - \left(1-M_\infty^2\right)\delta u^2\right] ds \\ &\quad + O\left(\delta^3\right) \end{aligned} \tag{17}$$

where $O\left(\delta^3\right)$ denotes the third and higher order terms. To reduce the integral of the drag expression to the wake, Maskell [19] introduced the idea of defining scalar functions ϕ and ψ for the cross-sectional velocities (v and w). ϕ and ψ are related to the trailing vorticity ζ and the velocity gradient σ through Poisson equations ($\Delta\psi = -\zeta$ and $\Delta\phi = \sigma$). ζ is assumed to be zero outside the wake. Maskell obtained:

$$\int_{\Sigma_1}\left(\delta v^2 + \delta w^2\right) ds = \int_{Wake}\frac{\psi\zeta}{U_\infty^2} ds - \frac{1}{S_{ref}}\int_{\Sigma_1}\frac{\phi\sigma}{U_\infty^2} ds \tag{18}$$

Consequently, the expression (17) becomes:

$$\begin{aligned} C_D &= \frac{1}{S_{ref}}\int_{Wake}\left[-\frac{2}{\gamma M_\infty^2}\delta P_i - \delta T_i \right. \\ &\quad \left. + \left(1-\frac{M_\infty^2}{4}\right)\delta T_i^2 - \delta P_i \delta T_i\right] ds \\ &\quad + \frac{1}{S_{ref}}\int_{Wake}\frac{\psi\zeta}{U_\infty^2} ds \\ &\quad - \frac{1}{S_{ref}}\int_{\Sigma_1}\left[\left(1-M_\infty^2\right)\delta u^2 + \frac{\phi\sigma}{U_\infty^2}\right] ds \\ &\quad + O\left(\delta^3\right) \end{aligned} \tag{19}$$

In this expression, each term, except the δu^2 one, can be clearly identified as due to reversible or irreversible effects which are respectively responsible for the lift-induced and the profile drag components. This δu^2 term is due to both effects and is responsible for both components. To guarantee an accurate drag breakdown, the axial velocity variations have to be divided into reversible and irreversible components. Moreover, to apply this formulation from wake measurements the domain of integration of equation (19) has to be reduced to the wake.

3.1.3 Axial velocity breakdown

To determine both axial velocity components, the flow is assumed without stagnation pressure and temperature variations. This assumption allows the evaluation of the reversible component δu^*. In these conditions the static pressure P^* and the axial velocity U^* are defined by :

$$\left\{ \begin{array}{l} P^* = P\left(P_i = P_{i\infty}, T_i = T_{i\infty}\right) \\ U^* = U\left(P_i = P_{i\infty}, T_i = T_{i\infty}\right) \end{array} \right. \tag{20}$$

From the isentropic relations, the static pressure can be expressed according to the velocity components :

$$\frac{P^*}{P_\infty} = \left(1 + \frac{\gamma-1}{2}M_\infty^2\left(1 - \frac{U^{*2}+v^2+w^2}{U_\infty^2}\right)\right)^{\frac{\gamma}{\gamma-1}} \tag{21}$$

The axial velocity is :

$$\frac{U^*}{U_\infty} = \left[1 - \frac{2}{\left(\gamma-1\right)M_\infty^2}\left(\left(\frac{P^*}{P_\infty}\right)^{\frac{\gamma-1}{\gamma}} - 1\right) - \frac{v^2+w^2}{U_\infty^2}\right]^{\frac{1}{2}} \tag{22}$$

From equation (16), the reversible and irreversible axial velocity variations are defined by :

$$\left\{ \begin{array}{l} U^* = U_\infty\left(1+\delta u^*\right) \\ \delta\overline{u} = \delta u - \delta u^* \\ U = U^* + \delta\overline{u}U_\infty \end{array} \right. \tag{23}$$

In the second part, the stagnation pressure and temperature variations are not assumed to be zero. In three dimensional compressible flows, the static pressure variations are not really affected by the viscous and wave effects in a wake plane. Consequently, the static pressure field P^* can be considered equal to the static pressure field P in the viscous flow. So, the reversible component δu^* of the axial velocity variations can be defined by :

$$\begin{aligned} \delta u^* &= \left[1 - \frac{2}{\left(\gamma-1\right)M_\infty^2}\left(\left(\frac{P}{P_\infty}\right)^{\frac{\gamma-1}{\gamma}} - 1\right) \right. \\ &\quad \left. - \frac{v^2+w^2}{U_\infty^2}\right]^{\frac{1}{2}} - 1 \end{aligned} \tag{24}$$

$\Im$ is defined in equation (15). From the isentropic relations, the static pressure can be expressed according to $\Im$ and the stagnation pressure field :

$$\frac{P}{P_\infty} = \frac{P_i}{P_{i\infty}}\Im^{\frac{\gamma}{\gamma-1}} \tag{25}$$

The expression (24) of the axial velocity variations becomes :

$$\begin{aligned} \delta u^* &= \left[1 - \frac{2}{\left(\gamma-1\right)M_\infty^2}\left(\left(\frac{P_i}{P_{i\infty}}\right)^{\frac{\gamma-1}{\gamma}}\Im - 1\right) \right. \\ &\quad \left. - \frac{v^2+w^2}{U_\infty^2}\right]^{\frac{1}{2}} - 1 \end{aligned} \tag{26}$$

The irreversible variations $\delta\overline{u}$ are defined by :

$$\begin{aligned}\delta\overline{u} &= \delta u + 1 \\ &\quad - \left[1 - \frac{2}{(\gamma-1)M_\infty^2}\left(\left(\frac{P_i}{P_{i\infty}}\right)^{\frac{\gamma-1}{\gamma}}\Im - 1\right)\right. \\ &\quad \left. - \frac{v^2+w^2}{U_\infty^2}\right]^{\frac{1}{2}} \end{aligned} \quad (27)$$

This definition guarantees that $\delta\overline{u}$ is zero outside the wake and that the breakdown can be carried out in all configurations without restriction because it can be shown that :

$$\begin{aligned}1 - \frac{2}{(\gamma-1)M_\infty^2}\left(\left(\frac{P_i}{P_{i\infty}}\right)^{\frac{\gamma-1}{\gamma}}\Im - 1\right) - \frac{v^2+w^2}{U_\infty^2} \\ \geq \frac{U^2}{U_\infty^2} \geq 0 \end{aligned} \quad (28)$$

To carry out the phenomenological drag breakdown, this definition has to be implemented in the drag equation (19).

3.1.4 Profile and lift-induced drag components

The previous axial velocity breakdown is introduced in equation (19) and the drag becomes :

$$\begin{aligned}C_D &= \frac{1}{S_{ref}}\int_{Wake}\left[-\frac{2}{\gamma M_\infty^2}\delta P_i - \delta T_i\right. \\ &\quad \left. + \left(1 - \frac{M_\infty^2}{4}\right)\delta T_i^2 - \delta P_i \delta T_i\right] ds \\ &\quad + \frac{1}{S_{ref}}\int_{Wake}\frac{\psi\zeta}{U_\infty^2}ds \\ &\quad - \frac{1}{S_{ref}}\int_{\Sigma_1}\left[\left(1-M_\infty^2\right)\left(\delta u^* + \delta\overline{u}\right)^2 + \frac{\phi\sigma}{U_\infty^2}\right] ds \\ &\quad + O\left(\delta^3\right) \end{aligned} \quad (29)$$

$\delta\overline{u}$ is zero outside the wake, the second integral can partially be reduced to the wake :

$$\begin{aligned}C_D &= \frac{1}{S_{ref}}\int_{Wake}\left[-\frac{2}{\gamma M_\infty^2}\delta P_i - \delta T_i\right. \\ &\quad \left. + \left(1 - \frac{M_\infty^2}{4}\right)\delta T_i^2 - \delta P_i \delta T_i\right. \\ &\quad \left. - \left(1-M_\infty^2\right)\left(\delta\overline{u}^2 + 2\delta u^*\delta\overline{u}\right)\right] ds \\ &\quad + \frac{1}{S_{ref}}\int_{Wake}\frac{\psi\zeta}{U_\infty^2}ds \\ &\quad - \frac{1}{S_{ref}}\int_{\Sigma_1}\left[\left(1-M_\infty^2\right)\delta u^{*2} + \frac{\phi\sigma}{U_\infty^2}\right] ds + O\left(\delta^3\right) \end{aligned} \quad (30)$$

The last term is still not a wake integral. To overcome this problem, the works of Cummings et al.[8] can be used. They related the gradient velocity term with the reversible axial velocity variations one:

$$\int_{\Sigma_1}\left(1-M_\infty^2\right)\delta u^{*2} ds = -\int_{\Sigma_1}\frac{\phi\sigma}{U_\infty^2}ds + O\left(\delta^3\right) \quad (31)$$

This relation can be applied because Cummings et al. defined their axial velocity variations from a flow without entropy and enthalpy variations. This is the definition of δu^*. As a consequence, this last term is zero to the second order, the drag expression can be reduced to the wake and the profile and lift-induced drag components can be identified:

$$\begin{aligned}C_{D_{pr}} &= \frac{1}{S_{ref}}\int_{Wake}\left[-\frac{2}{\gamma M_\infty^2}\delta P_i\right. \\ &\quad \left. - \delta T_i + \left(1 - \frac{M_\infty^2}{4}\right)\delta T_i^2 - \delta P_i \delta T_i\right. \\ &\quad \left. - \left(1-M_\infty^2\right)\left(\delta\overline{u}^2 + 2\delta u^*\delta\overline{u}\right)\right] ds \end{aligned} \quad (32)$$

$$C_{Di} = \frac{1}{S_{ref}}\int_{Wake}\frac{\psi\zeta}{U_\infty^2}ds \quad (33)$$

With this method, the crossing term $\delta u^*\delta\overline{u}$ is introduced in the profile drag, but this point is debatable. This term represents the interaction between the viscous and wave wakes and the reversible effects of the flow, so it can be defined in the profile or in the lift-induced drag. Physically, the order of magnitude of this term is lower than the δu^2 one because in the wake $\delta u^* << \delta u$ and $O\left(\delta\overline{u}\right) \sim O\left(\delta u\right)$. So, the contribution of this term to the drag is negligible and it can be attributed to both drag components without significant modification on the phenomenological drag breakdown.

Finally, this ONERA formulation provides a reliable drag breakdown in all configurations and its domain of integration is reduced to the wake which allows the reduction of the measurement areas in a wind tunnel. In the following part, this new formulation is applied in high-lift conditions.

3.2 High-lift configuration

Within the framework of the Eurolift II European project, drag extractions were carried out from numerical solutions and wake surveys on a generic high-lift configuration. This task aimed at evaluating the influence of a through flow nacelle on the viscous and lift-induced drag components in landing conditions (Mach number=0.174, lift coefficient $CL = 2.15$ and $Re_c \simeq 1.3\ 10^6$ with $c = 0.34708m$).

3.2.1 Far-field drag extraction from wake measurements

For the experimental part, two configurations, with and without nacelle (see installed model in figure 15 , were tested in the Airbus Deutschland Low Speed Wind Tunnel (LSWT) at Bremen. Wake measurements were realized with a five holes probe in both configurations. The experimental lift and drag extraction method was used to determine the different drag components from these wake surveys. Tables 4 and 5 exhibit a good coherence between balance measurements and the results from the wake surveys in terms of lift and drag components.

Figure 15: Half model KH3Y.

Balance	CL	CD
Conf1	2.13	-
Conf2	2.15	-
Conf2-Conf1	0.02	170

Table 4: Balance measurements

Wake	CL	CD	CD_v	CD_i
Conf1	2.10	100%	26.9%	73.1%
Conf2	2.16	100%	28.1%	71.9%
Conf2-Conf1	0.06	161	71	90

Table 5: Far-field drag values from wake surveys.

Table 5 provides a comparison between both configurations in terms of viscous CD_v, lift-induced CD_i and total CD drag components. The nacelle has a strong influence on the viscous component as expected (+71 drag counts), but also on the induced component (+90 drag counts) because of the increase of the lift and the modifications of the spanwise load.

Figures 16 and 17 compare the local and spanwise viscous and lift-induced drag distributions for both configurations. The local fields allow a very detailed study in terms of drag sources with a clear identification of the different parts of the wing : flap track fairings, gap between the wing and the fuselage, belly fairing and also discontinuities on the flap. The spanwise viscous drag distributions, in figure 16, show the influence of the nacelle on the whole wingspan and not only on its own viscous wake. In figure 17, the spanwise loads and lift-induced drag distributions provide very accurate information concerning the influence of the nacelle on the vorticity field. The supplement of lift and lift-induced drag results on the development of two counter rotating vortices in each side of the nacelle.

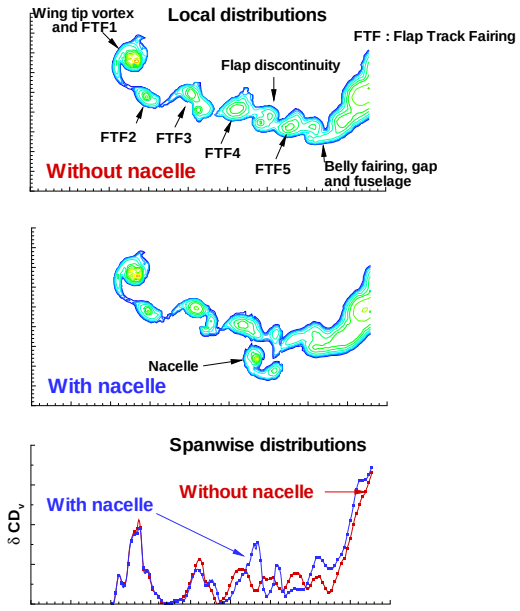

Figure 16: Local viscous drag fields and spanwise distributions from wake measurements.

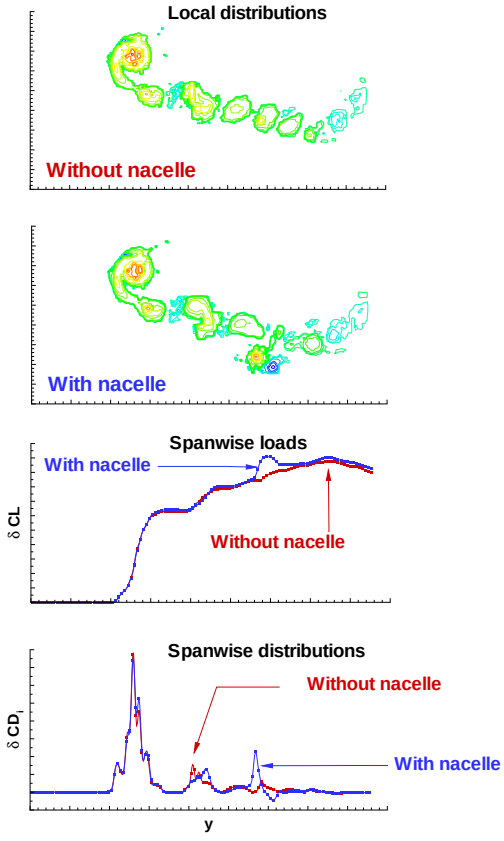

Figure 17: Local lift-induced drag fields, spanwise loads and spanwise lift-induced drag distributions from wake measurements.

3.2.2 Far-field drag extraction from numerical solutions

The numerical computations have been carried out by DLR using TAU code and analysed with drag extraction post-processor FFD72 within the framework of Eurolift II project.

As presented in table 6, the pressure drag is logically predominant (around 92%) on the friction drag. For these two high-lift cases, it appears that the near-field drag values (CD_{nf}) are overestimated in comparison to the experimental values.

TAU	CL	CD_p	CD_f	CD_{nf}
Conf1	2.16	92.3%	7.7%	100%
Conf2	2.17	92.0%	8.0%	100%

Table 6: TAU computations - Near-field drag values.

Remark on the pressure drag : this component results from an imbalance between pressure forces acting in the drag direction and in suction forces acting in thrust direction. On a three-element configuration, the numerical resolution must be optimal on all the aircraft lifting surfaces so that a desequilibrium between the two previous contributions (pressure drag and suction thrust) does not occur. If it is not the case, this may create a large over-prediction of drag. For example, if the suction peak is not correctly captured on the slat, the flap drag will be preponderant and the pressure drag will be over-evaluated.

FFD72 drag extraction post-processor was used to evaluate viscous and lift-induced drag (see table 7) and to analyse the flow field.

One main difficulty with high-lift cases is to separate spurious drag from physical drag. Indeed, high curvature zones as wing and slat leading edges regions, which are responsible for a large part of the spurious drag productions (as indicated in the first part of this paper), are embedded in high turbulent viscosity values coming respectively from the slat and wing trailing edges. This implies that these numerical productions are detected as viscous shear layers by the post-processing method leading to an over-estimation of the viscous drag component. Further developments will be devoted to this particuliar point specific to high-lift configurations.

A comparison of the far-field drag breakdown obtained from LSWT wake surveys and from TAU computations (see tables 5 and 7) exhibits a large difference in the drag values. However, tendencies are the same : for the installed configuration the percentage of viscous drag increases while the percentage of lift-induced drag decreases within the total drag balance. It is very interesting to notice that the induced drag ($63 - 73\%$ of the total drag) is preponderant on the viscous drag ($27 - 35\%$) in landing condition.

TAU/FFD72	CL	CD	CD_v	CD_i
Conf1	2.16	100%	32.7%	66.7%
Conf2	2.17	100%	35.6%	63.8%

Table 7: Far-field drag extraction from TAU computations.

The influence of the flap track fairings, nacelle, slat/gap/inner wing zone and wing tip swirling region on the spanwise viscous drag distributions is cleary visible on figure 18. The nacelle has a very local effect and does not seem to affect the inner and outer part of the wing in this low-speed case. For the installed configuration, the two vorticity sources produced on the lateral sides of the nacelle lead to a local increase of the friction and viscous pressure drag with a stronger intensity for the outer vortex. This kind of plot should be very useful for designers to evaluate the impact of different shapes on the drag distributions along the wing span not only in landing conditions but also in take-off and cruise conditions.

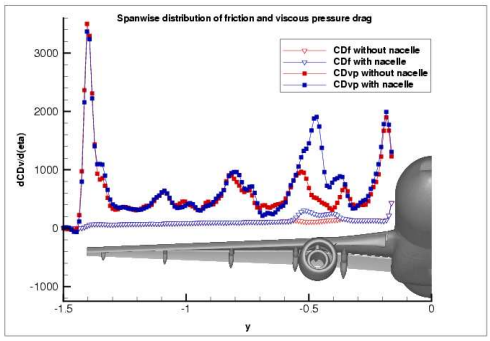

Figure 18: Spanwise distribution of friction and viscous pressure drag.

Currently, the post-processing of such high-lift configuration from CFD computations still remains a hard stuff and needs more experience to provide more reliable drag breakdown especially in regards to the elimination of the non negligible productions of spurious drag.

3.2.3 Discussion

Some uncertainties remains concerning the experimental and numerical results :

• Half-model is not well suited to define absolute drag values.

• Interaction between the vorticity field and the wind tunnel boundary layer downstream of the wing for this high-lift configuration may modify the flow around the model.

• CFD computations should be analysed in detail to explain a non negligible drag scatter with the experimental values (same conclusion for Eurolift partners).

• For the post-processing, the method is not yet able to separate and eliminate all the spurious drag productions from physical ones. This implies that for high-lift configurations, the far-field drag breakdown may be "polluted" by spurious productions.

4 Conclusions

This paper presents a survey of recent activities at ONERA concerning the far-field drag extraction from numerical solutions and wake measurements. Within the framework of the ONERA-DLR cooperation, the post-processing of structured elsA and hybrid TAU solutions allows to obtain interesting cross-comparisons and reliable drag breakdown on transonic configurations. Furthermore, the original far-field drag extraction from wake surveys allows to determine the different drag components and to evaluate the influence of a nacelle on the viscous and lift-induced drag components for a configuration in landing conditions. The drag extraction from numerical solutions, reliable for transonic configurations, needs more developments for high-lift cases even if it provides a very useful and detailed field analysis.

Acknowledgments

The authors would like to thank D.Destarac for his assistance and his thorough review of this paper.

References

[1] J.W.Slooff, *Computational Drag Analysis and Minimization (Mission Impossible ?),* AGARD-R-723, 1985.

[2] J.van der Vooren and D.Destarac, *Drag / Thrust Analysis of Jet-propelled Transonic Transport Aircraft; Definition of Physical Drag Components,* Aerospace Science and Technology Vol.8, N^o7, October 2004.

[3] D.Destarac, *Far-Field / Near-Field Drag Balance Applications of Drag Extraction in CFD,* Lecture Series 2003-02, VKI, Belgium, February 2003.

[4] S.Esquieu, *Aircraft Drag Extraction from Patched Grid Computations,* 21st AIAA Applied Aerodynamics Conference, Orlando (USA), AIAA-2003-3659, June 23-26, 2003.

[5] R.Tognaccini and L.Paparone, *Drag Breakdown and Drag/Thrust Bookkeeping from CFD Calculations, Workshop on European Research on Aerodynamic Engine/Airframe Integration for Transport Aircraft,* Braunschweig, Germany, 2000.

[6] R.Tognaccini, *Methods for Drag Decomposition, Thrust-Drag Bookkeeping from CFD Calcul ations,* Lecture series CFD-Based Aircraft Drag Prediction and Reduction 2003-02, VKI, 2003.

[7] D.Destarac, *Drag Extraction from Solutions of the Euler and Navier-Stokes Equations,* Extended Abstract, 1st ONERA-DLR Aerospace Symposium, Paris, France, 1999.

[8] R.M.Cummings, M.B.Giles and G.N.Shrinivas, *Analysis of the elements of drag in three-dimensional viscous and inviscid flows.* AIAA Paper 96-2482, 1996.

[9] S.Esquieu, *Validation of elsA-structured and Tau-hybrid RANS codes,* RT 1/08961 DAAP, December 2004.

[10] L.Cambier and M.Gazaix, *elsA : an efficient object-oriented solution to CFD complexity.* AIAA 2002-0108, Reno, Jan.2002.

[11] M.Gazaix, A.Jolles and M.Lazareff, *The elsA Object-Oriented Computational Tool for Industrial Applications.* ICAS Congress, 2002.

[12] T.Gerhold, M.Galle, O.Friedrich and J.Evans, *Calculation of Complex Three-Dimensional Configurations employing the DLR-TAU-Code.* AIAA, 1997.

[13] S.Melber-Wilkending, R.Wilhelm and H.F. von Geyr, *RANS Solutions for a Complex High-Lift Configuration of a Transport Aircraft with Engine Including Improved Resolution of the Nearfield,* AIAA, 2004-5081, 2004.

[14] B.Mialon, *Exploitation of transonic tests of the AS28 wing-body configuration in DNW-HST, ETW and S1MA wind tunnels.* RT 212/03222 DAAP - ONERA, Dec. 2003.

[15] V.Schmitt and D.Destarac, *Recent Progress in Drag Prediction and Reduction for Civil Transport Aircraft at ONERA,* AIAA 98-0137, Jan.1998.

[16] V.Berg et D.Destarac, *Les Méthodes de Calcul et d'Analyse de la Trane : Des Outils pour les Concepteurs de Formes Aérodynamiques,* 32eme Colloque AAAF, Lyon, 1996.

[17] M.Méheut and D.Bailly, *Drag Prediction and Wake Survey Techniques.* CEAS Katnet Conference on Key Aerodynamic Technologies, Bremen (Germany), 20-22 June 2005.

[18] M.Méheut and D.Bailly, *Profile Drag Formulations and Drag Breakdown from Wake Measurements.* 24th AIAA Applied Aerodynamics Conference, AIAA-2006-3166, San Francisco, June 2006.

[19] E.C.Maskell, *Progress towards a method of measurement of the components of the drag of a wing of finite span.* RAE TR 72232, 1972.